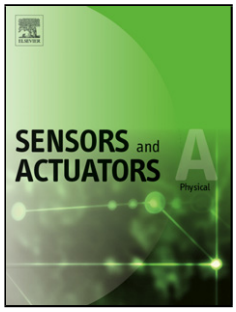

Title: Road surface condition detection utilizing resonance frequency and optical technologies

Authors: Kang Gui, Lin Ye, Junfeng Ge, Faouzi Alaya Cheikh, Lizhen Huang

PII: S0924-4247(19)30099-8
DOI: https://doi.org/10.1016/j.sna.2019.111540
Article Number: 111540

Reference: SNA 111540

To appear in: *Sensors and Actuators A*

Received date: 17 January 2019
Revised date: 12 July 2019
Accepted date: 2 August 2019

Please cite this article as: Gui K, Ye L, Ge J, Cheikh FA, Huang L, Road surface condition detection utilizing resonance frequency and optical technologies, *Sensors and amp; Actuators: A. Physical* (2019), https://doi.org/10.1016/j.sna.2019.111540

Road surface condition detection utilizing resonance frequency and optical technologies

Kang Gui[a], Lin Ye[a], Junfeng Ge[a,b,c,*], Faouzi Alaya Cheikh[c], Lizhen Huang[d]

[a] *School of Artificial Intelligence and Automation, Huazhong University of Science and Technology (HUST), Wuhan, Hubei 430074, China*

[b] *National Key Laboratory of Science and Technology on Multispectral Information Processing, Wuhan, Hubei 430074, China*

[c] *Department of Computer Science, Norwegian University of Science and Technology (NTNU), Teknologivegen 22, 2815 Gjøvik, Norway*

[d] *Department of Manufacturing and Civil Engineering, Norwegian University of Science and Technology (NTNU), Teknologivegen 22, 2815 Gjøvik, Norway*

Graphical abstract

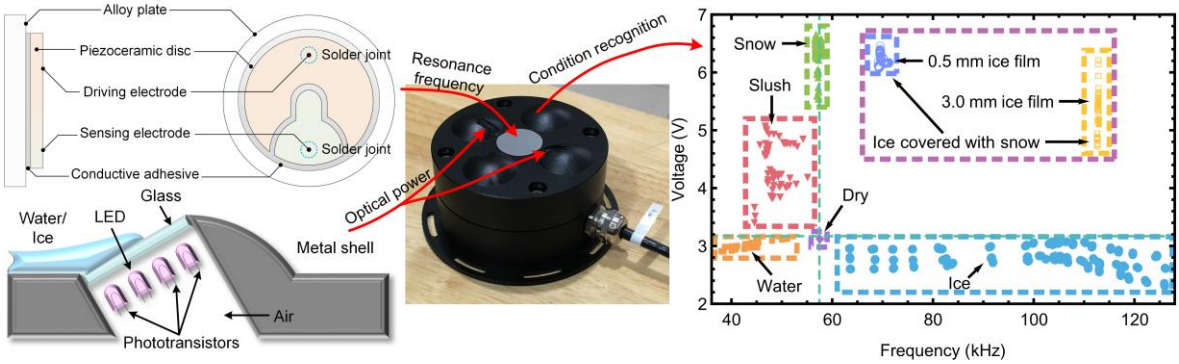

Research highlights

- Integration of two different sensors results in reliable recognition of six conditions.
- Different orders of resonance frequencies are evaluated for film thickness measurement.
- Optical power estimation model is constructed to study the optical property of ice, water and snow.
- A classification table is generated on the basis of the data distribution and proved in an outdoor test.

Abstract

With the booming development of road network and intelligent transportation systems, road surface condition information becomes more and more valuable in traffic accident prevention and route optimization. Although some existing embedded detectors have been providing road condition data in some regions, they are not functional enough in either complex condition recognition or film thickness measurement. This paper introduces a dual-sensor based road condition detector for six surface conditions with ice and water film measurement capability. The reflection type optical sensor and the piezoelectric sensor utilizing resonance technology are integrated in the detector. The finite element analysis was carried out to study the amplitude frequency response characteristics of the piezoelectric sensor and the optical power calculation model based on Fresnel Reflection was built to evaluate the output voltage of the optical sensor in different conditions. Several experiments were done to calibrate the detector and validate its performance. The results indicated that all of the 353 validation data points were correctly sorted and the measurement upper limit of the ice and water film was above 5 mm with accuracy better than 0.5 mm.

***Keywords*: Ice detection, optical sensor, resonance frequency, road surface condition, water film measurement**

Introduction

Adverse road surface conditions have bad impacts on traffic safety, mobility and transportation efficiency [1]. Slippery road conditions caused by water, ice and snow have led to fatal accidents around the world every year [2]. To reduce the potential injuries and traffic congestion, road surface condition detector has become one of the most significant infrastructures for road maintenance departments due to its indispensable role in providing timely road condition information and optimizing maintenance strategy. For instance, about 225445 tons of salt were used with 1610000 km driven while removing snow and ice on national and state roads during 2014 to 2015 winter in Norway and resulted in nearly 900 tons CO2eq emissions [3]. Maintenance work on this scale consumed huge amount of manpower and financial resources and caused wide range of pollution on account of gas emissions and overused deicing salt [4]. A road surface condition information network with enough detectors can help to plan a more environmentally friendly maintenance solution and thus reduce the consumption of deicing salt as well as manpower.

On the other hand, along with the rapid implementation of intelligent transportation concept, more and more detectors are needed on the roads and higher requests have been brought forward for advanced road condition detection. At present, diverse technologies are employed to detect road conditions. Non-contact detectors based on multispectral [5-7], polarization optics [8, 9] and combination of visual image and weather data [10] have been proposed. These detectors are designed to be installed on the automobiles or on the poles beside the roads. Most of them are accurate enough to distinguish icy, snowy, wet and dry surfaces, and some are able to cover a relatively larger area. Casselgren and his colleagues [5] proposed a road condition analysis system based on an infrared camera and a multispectral illumination module. Three different wavelengths of infrared light illuminated on the road surface with an incident angle of 45 degrees, and the camera was aimed at 30 degrees vertical angle. The system can classify dry, wet, icy and snowy asphalt with promising accuracy and is immune to the ambient light due to proper compensation. Jonsson [10] developed a model utilizing camera images as well as road weather variables to achieve a more accurate and relatively cost-effective non-contact road condition classification. Partial least squares and neural network were applied in the method, the model had a high percentage of correct recognition and the potential for optimization.

Casselgren’s system and Jonsson’s method are typical among non-contact road condition detectors, however, there are still problems to be solved. For instance, non-contact detectors can hardly measure the thickness of ice or water film which indicates that they can’t assess the severity of icy and flooded road condition. Meanwhile, if black ice is covered with snow, the detectors will be unable to recognize the icy condition. And the accuracy of non-contact methods is more likely to suffer from foggy, rainy weather as well as the deviation of installation angle and height. Furthermore, the price of such commercial systems is unaffordable for widespread use.

To a certain extent, embedded measurement method is complementary to non-contact detectors. Sensors based on conductivity and capacitance measurement have already been applied to the road [11-13]. Tabatabai and Aljuboori [11] implemented a novel concrete-based conductivity sensor for ice and water detection. The sensor is compact and the output is an effective basis for the classification of ice, wet and dry conditions. Troiano and his team [12] made an integrated capacitance sensor, driven at different frequencies and capable of distinguishing the three basic conditions. Nevertheless, the capacitance and conductivity of water, ice and snow can be affected by many factors. For example, deicing salt has great impact on the electrical properties of ice and water. Additionally, the change in temperature, film thickness and duration of freezing can result in a drift of the output. Taking long-term freezing ice layer as an example, it’s hard for the sensors to tell this condition apart from dry condition. In conclusion, conductivity and capacitance sensors meet the basic needs of road condition detection, but for further progress, such as film thickness measurement and additional condition recognition, new methods

must be applied.

For ice detection and thickness measurement, resonance sensor and optical sensor have been successfully applied in the field of aerospace. BF Goodrich Model 871 is an aviation ice sensor [14]. The probe is driven by the electromagnetic vibration system and can detect ice with high sensitivity, which is good for thickness measurement. However, the probe is too long to be installed on roads. Meanwhile, Ikiades and his team [15, 16] have investigated the optical methods for aviation ice detection. The reflected and scattered lights were utilized to measure the thickness and type of ice, which is very inspiring. Moreover, the similar principle can also be used for snow recognition. However, the complex road surface condition detection requires a more targeted approach, and the combination of these two technologies has great potential.

Under such circumstances, this paper introduces an embedded detector composed of piezoelectric and optical sensors. It integrates the advantages of both sensors and achieves a more efficient function via the complementation of their different recognition capabilities. Thus, the detector achieves the goal of classifying six road conditions (including dry, water, dry snow, slush, ice, ice covered with snow) and measuring ice and water film thickness with the upper limit higher than 5 mm.

Methods

A. Piezoelectric sensor

The detector consists of the piezoelectric sensor and the optical sensor. The piezoelectric sensor is designed for water and ice film measurement. According to the definition of natural vibration frequency, the ratio of stiffness and mass decides the value of resonance frequency, and the stiffness can be indicated by equivalent bending modulus in certain mechanical model. The ice film increases both the equivalent bending modulus and the mass of the sensor, whereas the water film only increases the mass. Consequently, it turns out that the ice film significantly increases the resonance frequency of the sensor, the water film decreases it and dry snow slightly decreases it.

Based on this theory, Roy *et al*. [17] implemented an ice sensor utilizing the vibration characteristic of a metal plate. Piezoelectric transducer (PZT) was attached to the metal plate as the actuator and sensing element. Direct piezoelectric as well as adverse piezoelectric effects were utilized to measure the 1^{st} order resonance frequency of the sensor. With one piece of piezoceramic driving the metal plate to vibrate and the other measuring the vibration amplitude through adverse piezoelectric effect, the sensor is able to collect the resonance frequency data. Thus, it is capable of measuring the thickness of ice and water films. However, the measurement range is from 0 mm to 0.5 mm, which is too small for road application. Li *et al*. [18] enlarged the measurement range by redesigning the sensor and extending the diameter of the vibration part from 15 mm to 45 mm, the upper limit of the measurement range increased to 1.4 mm for the ice film and 8 mm for the water film. But this structure leads to another problem. The thickness of the sensor's vibration part is only 0.0127 mm, and the diameter thickness ratio is so small that the sensor can be heavily damaged when automobiles run over. Roy's and Li's research offers a new strategy to measure ice and water on the road. In fact, this kind of piezoelectric sensor can achieve larger and more reliable measurement by optimizing the measurement method.

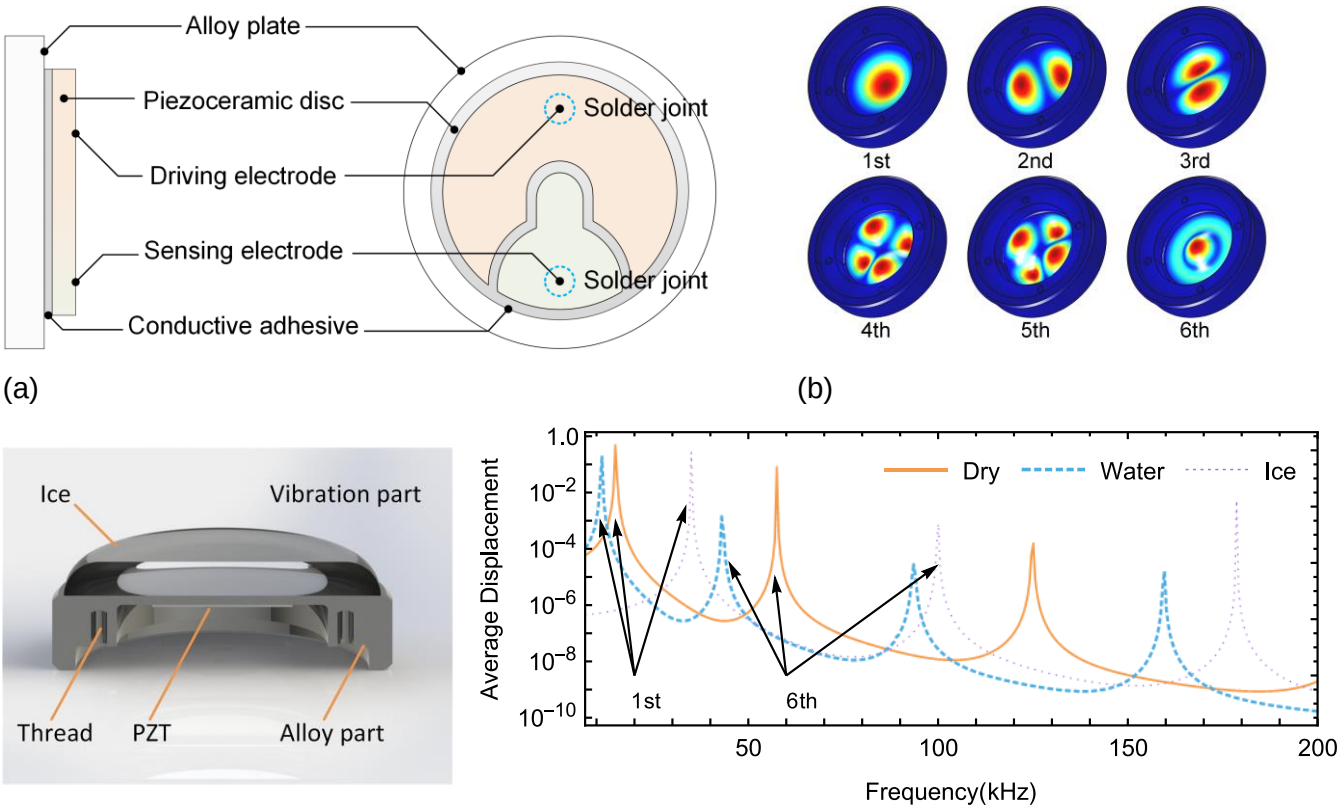

Figure 1. (a) The sketch map of piezoelectric sensor's vibration part, and the screw thread of the alloy part has been omitted. (b) The bottom view of simulated no-load mode shapes from the 1st order to the 6th. The displacement of the dark blue part is zero, and the dark red part represents the maximal displacement region. (c) The cross section view of the sensor's vibration part. (d) The normalized amplitude frequency response curves in log coordinates from FEA.

Roy and Li used the 1st order resonance frequency of the sensor to calculate the thickness of ice and water films. This method restricts the measurement range on account of the increasing damping when ice grows thicker. On this occasion, the amplitudes of some peaks decrease rapidly and eventually lead to the failure of locating peak position and the instability of sensor reading. To overcome this limitation, finite element analysis (FEA) based on COMSOL Multi-physics has been done to figure out the amplitude frequency response characteristic of the piezoelectric sensor in the previous study [19].

On the basis of the previous work, the structure of the sensor is optimized. The sketch map of optimized piezoelectric sensor's vibration part developed in this paper is shown in Fig. 1(a). The metal plate is made of constant elasticity alloy and serves as the upper shell of the piezoelectric sensor. To protect the sensor from being crushed, the plate is designed to be rather thick and small.

In this case, the thickness and the diameter of the vibration part have been set as 0.45 mm and 16.9 mm respectively. The diameter of the sensor itself is 25.4 mm, and more than 5.5 mm depth screw thread as well as conductive adhesive are used to firmly fix the sensor on a much larger metal shell.

On the other hand, the alloy plate is connected to the ground of the sensor circuit so that the electric current on driving and sensing electrodes can each form a loop. The sensor is driven with frequency scanning signal and the amplitude frequency response curve is collected via sensing electrode.

The simulated no-load mode shapes from the 1st order to the 6th order are shown in Fig. 1(b), with the vibration part locating in the center of the sensor. A piezoelectric disk polarized in the thickness direction has been used in the sensor, and the excitation electric field is applied in the thickness direction. Thus, the vibration

propagates along the radial direction due to the basic properties of the elastomer. Under these circumstances, according to the knowledge of vibration excitation, and in the absence of nodal lines (namely n = 0 in the Bessel equation), the 2nd order to 5th order vibration modes from FEA shown in Fig. 1(b) won't be generated. So, the 1st order and 6th order modes are important for the measurement in the limited excitation frequency band.

In general, these two modes are axisymmetric, and the maximum displacement is at the center of the plate. Based on piezoelectric effect, the maximum displacement generates the maximum amount of charge, and thus the sensing electrode should occupy this area for the increasing of sensitivity. However, the driving electrode and sensing electrode need to be connected to the printed circuit board by wires, and the mass and bending modulus brought by solder joints will affect the vibration. To solve this problem, in the electrode shape design, the solder joints are set at the edge of the piezoelectric disk, as is shown in Fig. 1(a). Enough space has been reserved in the sensing electrode area for the soldering operation.

The size of the piezoelectric disk should be within a reasonable range. If the diameter is too large, it will make the disk easy to break. Additionally, the radius of the 6th order mode's inner nodal circle is about 0.38R based on elastic mechanics principles. Hence, large disk will result in the attenuation of the corresponding resonance peak. On the other hand, a small diameter will lead to weak piezoelectric effect. Meanwhile, the disk shouldn't be thick, because the mass and the bending modulus will affect the vibration. Under the guidance of these principles, the piezoelectric disk is designed for the proof-of-principle study in this paper. After the comparison of different sizes of disks, the dimensions of the piezoelectric disk are set as Φ12*0.2 (mm).

Different conditions have been simulated in COMSOL. As is shown in Fig. 1(d), amplitude frequency response curves of dry surface, 4 mm water film and 2 mm ice film from FEA are plotted. The average displacement values of the sensor's upper surface are normalized in log coordinates for a clear view. The frequency scanning ranges from 7 kHz to 200 kHz with a step length of 50 Hz, and it's obvious that the peaks of the curves shift to a lower frequency section with water accretion and move to higher frequency section with ice growing. The 1st and the 6th order peaks are remarkably high, whereas the other four peaks are not detected, which confirms the inference above.

B. Optical sensor

In addition to dry, water and ice, there are three snow conditions to be recognized. When snow falls on a dry surface, it's called dry snow condition (abbreviated as snow). If the snow partly melts into ice-water mixture, it's stated as slush condition. And if the snow layer covers an ice film, it's stated as ice covered with snow condition (abbreviate as covered).

The optical sensor is designed for snow detection. It consists of an infrared LED, a phototransistor array, a glass plate and a metal shell, as is shown in Fig. 2(a). The curvature of the water film and ice layer does appear occasionally. According to Snell's Law and Fresnel's Formula, the curvature may affect the light intensity reflected back to the phototransistor array. However, in the theoretical analysis stage, this effect will be ignored for its limited influence and model simplification, and optimization measures will be taken during the implementation.

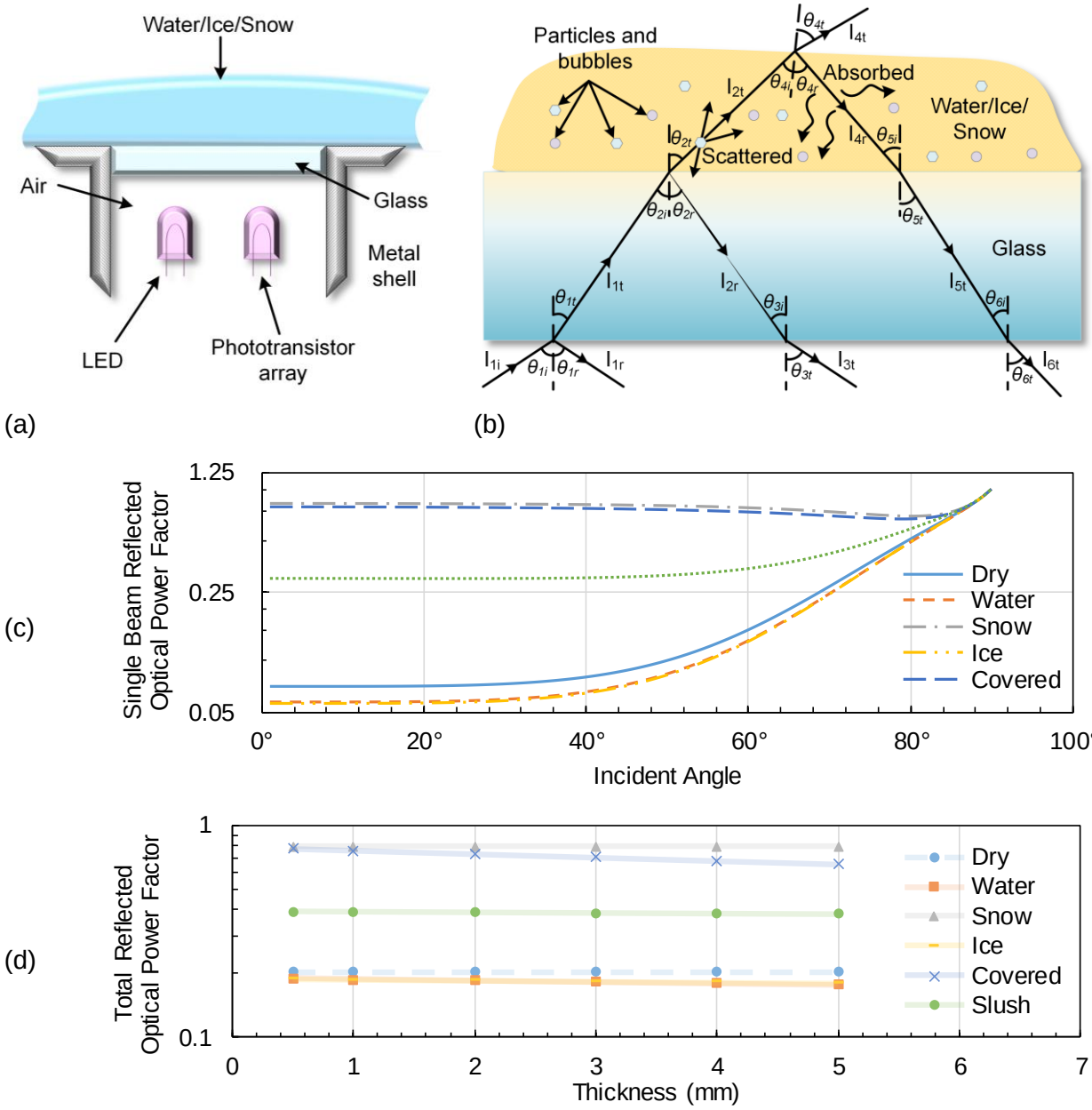

Figure 2. (a) The schematic view of the optical sensor consists of an infrared LED and a phototransistor array. (b) A typical beam path of the optical sensor, and multiple reflections in the same optical medium are omitted. (c) The calculated single beam reflected optical power factor in log coordinates of each incident angle from 0 degree to 90 degrees, and six different surface conditions are considered. (d) The estimated total reflected optical power factor in different thickness conditions.

Inside the sensor, the LED has a narrow beam angle of 30 degrees and emits modulated light of 1 kHz, so that most of the light energy is concentrated at a small incident angle. And the phototransistor has a wide field angle of 120 degrees and the array further extends the field of view. Generally, the light received by the array is from three sources: the modulated light which travels from the LED into the array directly, the ambient light from the environment and the modulated light reflected (including scattered light) from the glass and the loads. The LED is fixed next to the phototransistor array, and a narrow beam angle will help reduce the power of light which travels from the LED into the array directly.

In the meantime, the modulated light which travels directly into the phototransistor array has been measured and filtered in the signal processing circuit, and the ambient light from the environment is perfectly filtered through demodulation. Thus, the reflected optical power is collected as an indicator of load type.

Fig. 2(b) shows a typical beam path of a random angle incident light I_{1i} in the glass plate and load medium. Multiple reflections in the same optical medium are omitted for simplification. Specifically, when the light beam propagates through the ice layer or water film, it will be refracted, reflected, partly absorbed, and scattered, as is shown in Fig. 2(b). According to Snell's Law, the main propagation path of the beam in the optical medium is predictable, and the optical power on the path can be estimated through Fresnel's Formula, Beer-Lambert's Law and Mie Scattering Theory.

Snell's Law and Fresnel's Formula are utilized to calculate the optical energy flow reflectivity and transmissivity on the beam path. The S polarized light and P polarized light are calculated separately through equation (1), where θ_i is the incident angle from the medium with the refractive index n_i, and θ_t is the refraction angle into the medium with the refractive index n_t, R_S and T_S are the reflectivity and the transmissivity of S polarized light, and R_P and T_P are the reflectivity and the transmissivity of P polarized light.

$$\begin{cases} n_i \sin\theta_i = n_t \sin\theta_t \\ R_S = \dfrac{\sin^2(\theta_i - \theta_t)}{\sin^2(\theta_i + \theta_t)} \\ R_P = \dfrac{\tan^2(\theta_i - \theta_t)}{\tan^2(\theta_i + \theta_t)} \\ T_S = \dfrac{\sin 2\theta_i \sin 2\theta_t}{\sin^2(\theta_i + \theta_t)} \\ T_P = \dfrac{\sin 2\theta_i \sin 2\theta_t}{\sin^2(\theta_i + \theta_t)\cos^2(\theta_i - \theta_t)} \end{cases} \tag{1}$$

Then, in accordance with Beer-Lambert's Law, the absorption of the optical energy flow is described in an exponential form. Equation (2) shows the relationship between incident light intensity I_i and transmissivity light intensity I_t from the perspective of absorption, where h is the thickness of the ice layer or water film, x is the distance light that travels in it, and a stands for the absorption coefficient. This relationship is still applicable in the optical energy flow.

$$\begin{cases} I_t = I_i e^{-ax} \\ x = \dfrac{2h}{\cos\theta_t} \end{cases} \tag{2}$$

On the other hand, scatter effects must be considered. Mie Scattering Theory can be used to describe the forward scatter attenuation of the energy flow. The optical power at any position of the beam path can be estimated by calculating the incident optical power decay at an infinitesimal distance Δx. In equation (3), Q_s is the scattering efficiency factor, which shows the proportion of energy loss due to scattering effects. K is the spatial density of the particles and bubbles of radius r. P_i is the incident optical power at any angle, and $P_i(x)$ is the optical power at distance x.

$$\begin{cases} P_i(\Delta x) = P_i(x) - P_i(x + \Delta x) = P_i(x) Q_S \pi r^2 K \Delta x \\ P_i(x) = P_i e^{-Q_S \pi r^2 K x} \end{cases} \tag{3}$$

Obviously, the form of the forward scatter attenuation is similar to that of the absorption effect. Thus, in equation (4), the optical power decay in glass plate is denoted as η_g and in water/ice is denoted as η_l, where a is the absorption coefficient and b is the scattering coefficient. There are six refractions in Fig. 2(b) labeled from one to six, and in total three beams contribute to the reflected light intensity I_r, denoted as I_{1r}, I_{3t} and I_{6t}. The upper surface of the load layer is parallel to the glass plate's upper surface, and the LED emits non-polarized light. Under such circumstance, S and P polarized lights are assumed to contribute the same intensity during the detection. Equation (4) describes the relationship between incident and reflected optical power in six different conditions, where P_i is the incident optical power at any angle, and P_s is the corresponding reflected optical power.

$$\begin{cases} P_{s\_dry} = P_i\left(R_{K1} + T_{K1}R_{K2}T_{K3}\eta_g\right) \\ P_{s\_snow} = P_i\left(R_{K1} + T_{K1}R_{snow}T_{K3}\eta_g\right) \\ P_{s\_water} = P_i\left(R_{K1} + T_{K1}R_{K2}T_{K3}\eta_g + T_{K1}T_{K2}R_{K4}T_{K5}T_{K6}\eta_g\eta_l\right) \\ P_{s\_ice} = P_i\left(R_{K1} + T_{K1}R_{K2}T_{K3}\eta_g + T_{K1}T_{K2}R_{K4}T_{K5}T_{K6}\eta_g\eta_l\right) \\ P_{s\_covered} = P_i\left(R_{K1} + T_{K1}R_{K2}T_{K3}\eta_g + T_{K1}T_{K2}R_{snow}T_{K5}T_{K6}\eta_g\eta_l\right) \\ P_{s\_slush} = P_i\{R_{K1} + T_{K1}[\gamma T_{K3}\eta_g + (1-\gamma)(R_{K2}T_{K3}\eta_g + T_{K2}R_{K4}T_{K5}T_{K6}\eta_g\eta_l)]\} \\ \eta_g = e^{-(a_g+b_g)x_g} \\ \eta_l = e^{-(a_l+b_l)x_l} \\ R_K = (R_S + R_P)/2 \\ T_K = 1 - R_K \end{cases} \tag{4}$$

In snow condition, the reflectivity R_{snow} is set as 90% according to snow's spectral reflectance data from United States Geological Survey. And in slush condition, the model is considered as a combination of snow and ice, part of the light being reflected directly by the loose structure and other light beam traveling through slush. The proportion of reflected light is denoted as γ, and it is set as 30% to describe a typical situation.

Table 1.

Related parameters of the single beam reflected optical power factor model.

	Air	Glass	Water	Ice	Slush
Refractive index	1.000	1.490	1.333	1.309	1.309
Absorption coefficient (cm^{-1})	0.00001	0.1	0.3	0.1	0.1
Scattering coefficient (cm^{-1})	-	0.01	0.01	0.1	0.1

Thus, given a certain incident angle, the single beam reflected optical power factor in different conditions can be calculated, as is shown in Fig. 2(c). The single beam reflected optical power factor in the figure is the ratio of the corresponding reflected optical power P_s and the incident optical power P_i, and the related parameters are listed in Table 1. The calculation results show that ice and water films will decrease the power of the light received by the phototransistor array, whereas snow layer will significantly increase it. And the difference between the conditions with and without a snow layer is very obvious when the incident angle is beneath 60 degrees. Apparently, the optical sensor can distinguish snow related conditions and water/ice conditions. And the total reflected optical power factor can be obtained by integration.

As for the backscattering effect, it will increase the reflected optical power, and consequently the difference between the dry condition and water/ice conditions will be reduced. The backscattering intensity is affected by the volume and spatial density of the particles and bubbles, which are difficult to quantify. According to the Mie Scattering Theory, the backscattering intensity varies greatly with particle size and illumination wavelength. Thus, the meaning of solving the scattering intensity distribution is limited in the case where the particle size and position distribution of the scattering particles cannot be accurately described. Meanwhile, a tilt mounting structure has been designed in the prototype of the detector. This structure will reduce the reflected optical power in water/ice conditions through the angle between glass plate and upper surface of water/ice films.

Assuming all the incident beams of different angles have the same light intensity, the total reflected optical power factor P can be calculated through:

$$P = \int_0^{90} P_s(\theta_i)/(P_i \times 90)\, d\theta_i \approx \sum_{\theta_i=0}^{\theta_i=90} P_s(\theta_i)/(P_i \times 90) \tag{5}$$

Fig. 2(d) lists the estimated total reflected optical power factor in different thickness conditions. With the film thickness growing in a certain range, the estimated total reflected optical power factor doesn't drift much.

Therefore, there will be a very large upper limit once the size and spatial density of micro bubbles and micro cracks stay in a reasonable range. According to the results, the thickness can influence the reflected optical power, but can't change the fact that a wide difference exists between the conditions with a snow layer and those without a snow layer. Besides, taking the narrow beam angle of the LED into consideration, most of the energy will concentrate in the incident beams with an incident angle lower than 15 degrees, which will increase the difference between these conditions.

Experiment

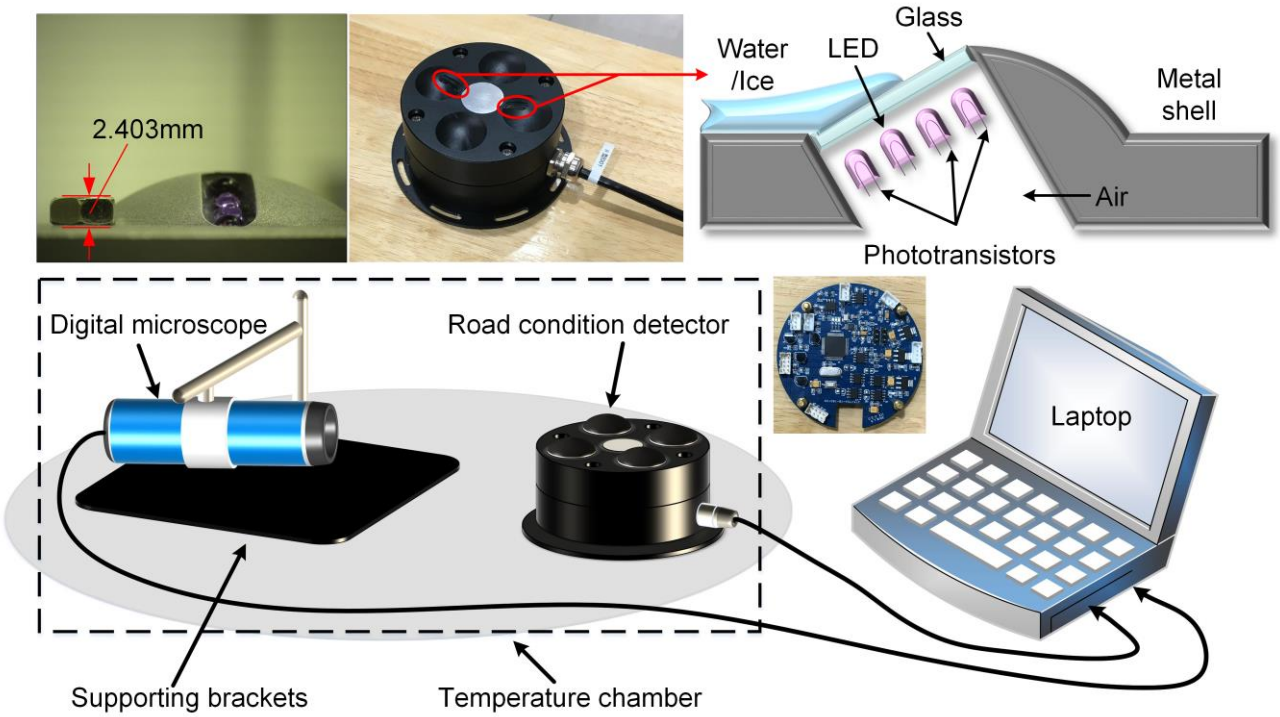

Figure 3. The experiment set up of road condition detector. A photo of the road condition detector is presented and the locations of the optical sensors are indicated with red circles. The calibration of the digital microscope is done with a given height screw nut.

Experiments were conducted in a temperature chamber with a compact road condition detector and a digital microscope, as is shown in Fig.3. The prototype detector consists of a piezoelectric sensor and two optical sensors, and the dimensions are Φ95×50 (mm). The silvery piezoelectric sensor is embedded in the center of the upper surface shell, and the optical sensors are embedded in the hemispherical structure to protect the sensors from rolling compaction.

A tilt mounting structure has been designed to reduce the adverse effects of load film curvature and increase the difference between dry condition and water/ice conditions. As is shown in the figure, in general, the upper surface of the water film and ice layer will not be parallel to the glass if the sensor is mounted at a small angle. To be more specific, the water film and ice layer will adhere to the glass because of the water tension. In accordance with the principle of geometrical optics, more light will be reflected to other directions instead of being received by the phototransistor array. And if there is too much water or ice drowning the glass, the light will still be reflected to elsewhere due to the horizontal upper surface of the water film or ice layer. Meanwhile, snow can easily cover the glass when it falls. In this way, the optical signals of ice and water conditions are lower than those of the theoretical model. The tilt mounting structure enhances the recognition ability of the optical sensor.

Also, tilted glass is good for self-cleaning in rainy days.

A printed circuit board with a microprogrammed control unit is installed in the metal shell of the detector to activate the sensors and collect data. In the embedded program, the frequency scanning range is from 7kHz to 200kHz with a step length of 50Hz. The 1st and 6th order frequencies are measured. On the other hand, the photoelectric signals from the phototransistor array are processed with a digital averaging filter and added up as another key feature. All these procedures are smoothly done within seconds, which means the data processing requirements are reasonably low.

A digital microscope was used to measure the thickness of the ice and water films on the upper surface of the piezoelectric sensor, Fig. 3 shows an image of the microscope calibration phase captured by it in the top left corner. The real height of the screw nut is 2.401 mm, and the measured result from the microscope is 2.403 mm. A laptop was used to display and restore the data from the detector and the images captured by the microscope.

All the six road conditions, including dry, water, dry snow, slush, ice, and ice covered with snow were tested during the experiment. The dry condition was tested at -10 degrees centigrade and 20 degrees centigrade with no-load on the detector's upper surface. The water condition was tested at 20 degrees centigrade with a uniform water film on the detector. The slush condition was tested at 0 degrees centigrade with melting snow layer on the detector. The snow, ice and ice covered with snow conditions were all tested at -10 degrees centigrade with corresponding loads on the detector. The thickness of all the films ranged from 0.2 mm to 8.0 mm. The 1st and the 6th order resonance frequencies of the piezoelectric sensor and the output voltages of the optical sensors were recorded. The test results were used to create a classification table to decide the surface condition of the detector, and then an outdoor validation test was conducted to prove the performance of the detector. The validation test was done at random ambient temperature and in various surface conditions.

Results and discussion

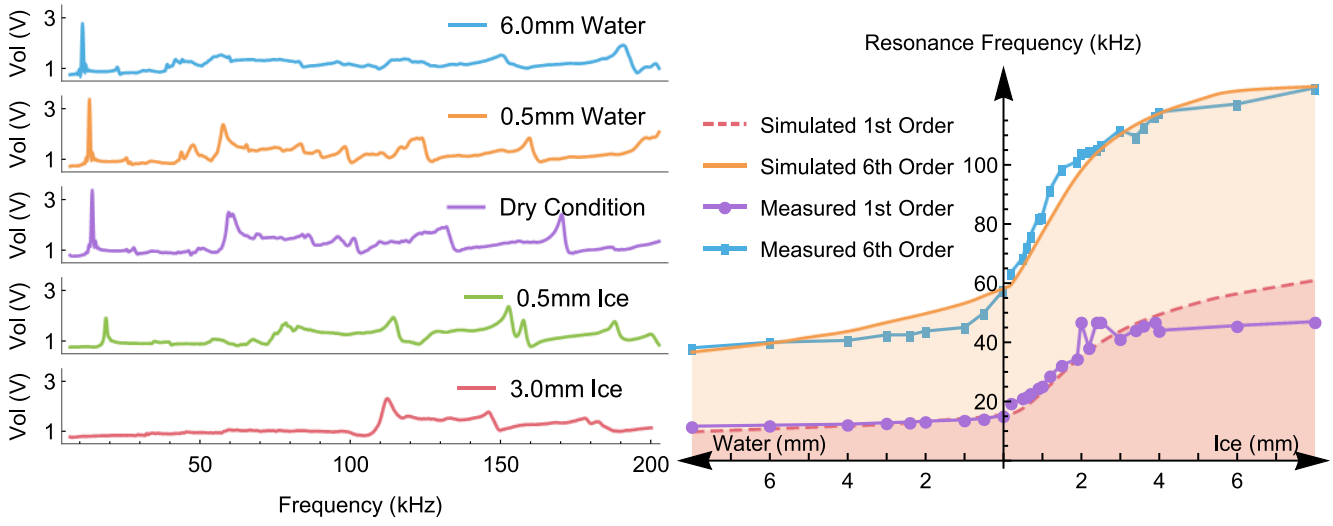

(a) (b)

Figure 4. (a) The amplitude frequency response curves of four typical conditions. (b) The simulated and measured calibration curves of the piezoelectric sensor.

The piezoelectric sensor works as an indicator of ice and water. The calibration work of it was done during the experiment, as is shown in Fig. 4. The amplitude frequency response curves in Fig. 4(a) present the shift process of the resonance frequency when ice and water films grew. The resonance peaks shifted to lower frequency section with water accretion and to higher frequency section with ice growing, which was consistent with the results of finite element analysis. Importantly, it's obvious that the 1st order resonance peak decreased

rapidly with ice accumulating. Thus, it was hard to locate the 1st order resonance frequency when the ice film was thick. Fig. 4(b) shows the simulated as well as the measured resonance frequency curves collected during the experiment. In total 30 sets of data were recorded in different test conditions, and the 1st and the 6th order resonance frequencies were plotted in the figure. In general, the simulated results matched with the experimental data, but two glitches appeared in the measured 1st order resonance frequency curve where the ice film thickness was about 2 mm to 3 mm. They were caused by the failure of locating the resonance peak, which was submerged in noisy background.

The curves in Fig. 4(b) suggest that the 1st order resonance frequency is hard to be detected when the ice film is thicker than 3.5 mm and the reading will hardly change with the growing of water when it's thicker than 4 mm. On the other hand, the 6th order resonance frequency performs larger dynamic range. In order to enhance the stability and extend the measurement range of the piezoelectric sensor, the 6th order resonance frequency is chosen as the indicator to measure the thickness of ice and water films.

Seven sets of different experimental conditions were tested in the temperature chamber, including dry, water, ice, dry snow, slush, 0.5 mm ice film covered with snow and 3.0 mm ice film covered with snow. Fig. 5 shows the data collected in six sets of adverse conditions. The two optical sensors' output voltages were added up for more accurate measurement. Photos of the six conditions show the typical surface condition of the detector during the experiment. Dry condition is included in the six subplots for its high stability and repeatability. The experiments were repeated for three times to obtain more comprehensive data and in total 1059 data points were collected. The average values are used in Fig. 5.

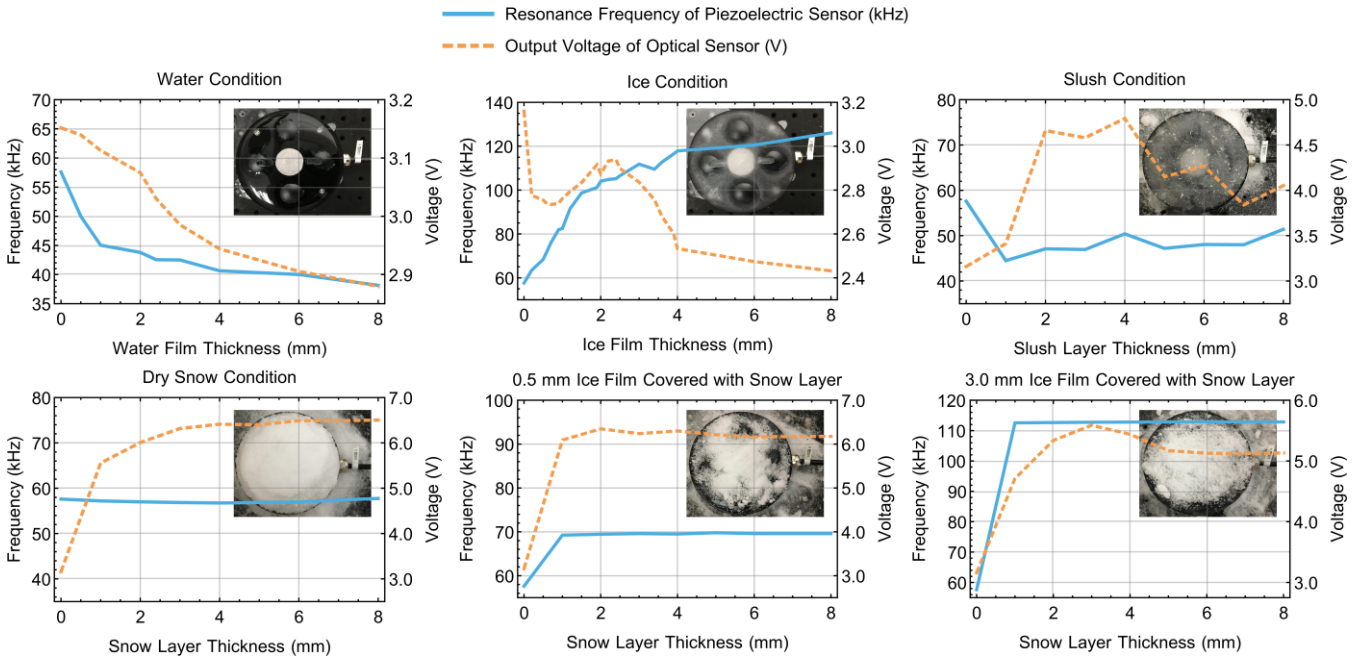

Figure 5. Average data values in six sets of different experimental conditions. The 6th order resonance frequency of the piezoelectric sensor and the output voltage of the optical sensor are shown. Photos of the experiment are placed in the corresponding subplot.

The curves in the figure illustrate the signal variation of the piezoelectric sensor's resonance frequency and optical sensor's output voltage. Compared with dry condition, optical voltage increased rapidly in snow related conditions (dry snow, slush, ice covered with snow), and decreased slightly in water and ice conditions. On the other hand, resonance frequency increased sharply in ice related conditions (ice, ice covered with snow), and decreased in water, snow and slush conditions.

The dry condition was tested at -10 degrees centigrade and 20 degrees centigrade with no-load on the detector's upper surface, and 100 data points were collected. The resonance frequency was stabilized around 57.5

kHz and the optical voltage was about 3.16 V during the whole test. The data suggest that the detector's output in dry condition is very stable.

The water condition was tested with 11 water films ranging from 0.5 mm to 8.0 mm, and 80 data points were collected. The resonance frequency decreased from 51.0 kHz to 38.0 kHz, and the optical voltage decreased from 3.13 V to 2.89 V. The curves are monotonic and become flat when the film thickness is above 4.0 mm.

The ice condition was tested with 21 ice films ranging from 0.2 mm to 8.0 mm, and 300 data points were collected. The resonance frequency monotonically increased from 63.2 kHz to 126.0 kHz overall, and the optical voltage decreased from 3.12 V to 2.32 V. The optical voltage rose again when the ice film grew to about 2 mm, which was caused by the irregular shape of the ice film. The ice formed on the glass plate of optical sensors always slightly bulged on account of the narrow semi-closed structure. As a result, more light was reflected to the phototransistor array when the thickness of the ice film was appropriate.

The dry snow condition was tested with 8 snow layers ranging from 1.0 mm to 8.0 mm, and 302 data points were collected. The resonance frequency varied within 2 kHz and the optical voltage increased from 5.54 V to 6.65 V. The reflection was very strong as expected, and the frequency shifted a little due to the mass added.

The slush condition was tested with 8 slush layers ranging from 1.0 mm to 8.0 mm, and 63 data points were collected. The resonance frequency varied in the range of 44.3 kHz to 54.9 kHz, and the optical voltage trembled in the range of 3.41 V to 5.10 V. Slush is a very complicated condition, the color of which can be white or more crystal, so the optical voltage turned out to be unstable but always higher than dry condition. And once part of the slush freezes into solid ice, the equivalent bending modulus become unpredictable. However, most part of the slush is still liquated, so the resonance frequency was always lower than dry condition and changed randomly.

The 0.5 mm ice film covered with snow condition was tested with 8 snow layers ranging from 1.0 mm to 8.0 mm, and 112 data points were collected. The resonance frequency stabilized around 69.3 kHz, and the optical voltage ranged from 6.08 V to 6.45 V. The 3.0 mm ice film covered with snow condition was tested with 8 snow layers ranging from 1.0 mm to 8.0 mm, and 102 data points were collected. The resonance frequency stabilized around 112.7 kHz, and the optical voltage ranged from 4.71 V to 6.22 V. The piezoelectric sensor responded to the ice films as analyzed. On the other hand, the optical voltage indicates the power of light received by the phototransistor array, and the ice covered with snow condition can be regarded as the combination of ice layer and dry snow. Snow is a strong reflector of light, so the optical voltage of dry snow condition is up to 6.5V. However, in the covered condition, the light beam may be scattered to other directions by the ice layer, and thus the optical voltage decreases to about 5V.

In summary, the data from the seven sets of experimental conditions are consistent with the notion of estimated reflected optical power in Fig. 2 and the finite element analysis results in Fig. 4. The light decay caused by scattering and refraction is successfully detected in ice and water conditions, whereas the light reflection turns out to be very strong in snow related conditions, which verifies that the method of utilizing optical sensors to distinguish snow from ice and water is working. And the piezoelectric sensor also performs well in detecting ice and water related conditions. The ice films greatly increase the equivalent bending modulus of the vibration system, so the resonance frequency rises quickly with the growing of ice. The slush and water mainly increase the mass of the vibration system, and thus the resonance frequency decreases with water and slush accretion.

The combination of these two methods puts the data points of the seven conditions into a two-dimensional space, as is shown in Fig. 6(a). The points of the same experimental condition from different batches of tests gather together in a certain region, as is presented by the dashed rectangles. All the regions don't overlap mutually, which makes it possible to recognize each condition in the plot with the coordinates of the collected data points.

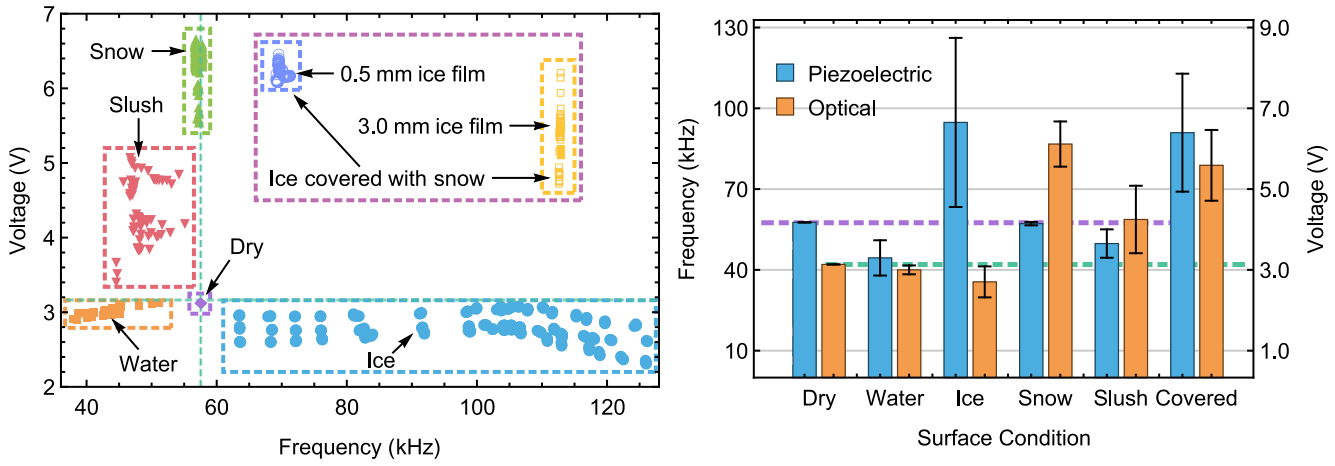

(a) (b)

Figure 6. (a) Data collected in seven sets of different experimental conditions. The data points of the same condition get together and stay in the same region. (b) The data ranges of the detector output from six surface conditions. The maximum and the minimum values are presented with error bars.

Among all the conditions, the dry condition is the most stable, with all the data points staying in one narrow region, and the coordinate of this region is set as the reference value for road condition classification. The data range is shown in Fig. 6(b), as the error bars indicate the maximum and the minimum values of each condition. Overall, the data ranges of different conditions suggest that all the other five conditions can be recognized by comparing the coordinates with the dry condition. To this end, the reference values of the dry condition coordinate are set as 57.5 kHz and 3.16 V respectively. Moreover, a section of 3 kHz wide and 0.30 V long around the reference coordinate is selected as dry region, so that the condition recognition process of the detector will be more stable and reliable.

Table 2.
Classification table of the detector.

	$f_r < 56\text{kHz}$	$56\text{kHz} \leq f_r \leq 59\text{kHz}$	$f_r > 59\text{kHz}$
$V_{opt} < 3.10\text{V}$	Water	Unknown	Ice
$3.10\text{V} \leq V_{opt} \leq 3.16\text{V}$	Water	Dry	Ice
$3.16\text{V} < V_{opt} \leq 3.40\text{V}$	Unknown	Dry	Unknown
$V_{opt} > 3.40\text{V}$	Slush	Dry snow	Ice covered with snow

Table 3.
Fitting functions and R-Squared values of the 6th order resonance frequency.

Order	Condition	Fitting Function (kHz)	R-Squared
Sixth	Ice	$0.0000747832x^3$-$0.018615x^2$+$1.56228x$-43.206	0.978315
	Water	-$0.00325644x^3$+$0.50532x^2$-$26.1039x$+449.382	0.981480
	Dry	$56 < x < 59$	-

As is shown in Table 2, the data field is divided into 12 regions based on the reference values and the dry section. The six road surface conditions are labeled in the nine regions and three remaining regions are labeled as unknown condition for no data points have been collected in such regions. As a result, 100% of the 1059 data points can be correctly classified into corresponding condition through Table 2, where f_r stands for the 6th order

resonance frequency obtained by the piezoelectric sensor and V_{opt} stands for the total optical voltage of optical sensors.

For the stability of the method, false signals must be considered. If the data falls into the unknown condition fields, the signals can be regard as false ones. More importantly, road surface conditions are relatively stable over a period of time, so in the embedded program of the detector, it will report the false signal situation if the condition changes rapidly or frequently.

On the other hand, the resonance frequency performs good repeatability in ice and water film thickness measurement and dry snow detection. So the resonance frequency is used to calculate the thickness of ice and water films. The film thickness measurement function was implemented by fitting the resonance frequency curves in Fig. 5, based on least square method. The fitted functions are shown in Table 3. R-Squared values are listed in the table to indicate the degree of fitting and the dry condition frequency band acts as a barrier to divide the ice and water frequency range. The results show that most of the fit residuals are lower than 0.3 mm, which guarantees the precision of the film thickness measurement.

An outdoor validation test was conducted with a concrete test road block to evaluate the performance of the classification table and the fitting curves, as is shown in Fig. 7. The test conditions were man-made and randomly chosen due to the warm weather of the city in which the test site located. In total 353 data points were collected. As is shown in Fig. 8(a), all the data points fit in the right sections divided on account of Table 2. The results validate the effectiveness of the classification table and prove the repeatability of the detector.

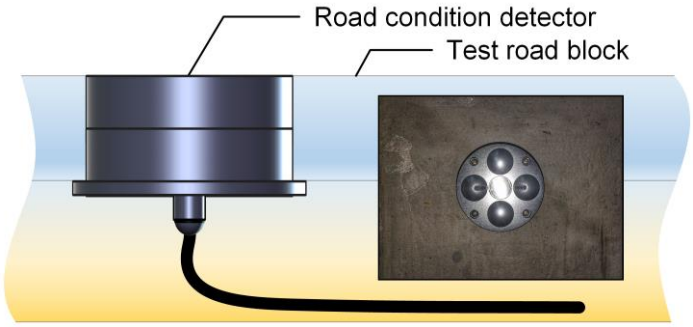

Figure 7. The installation sketch of the detector. The detector is installed in the hole of the test road block, and the cable lies in sandy soil beneath the concrete layer. A photo of the installed detector is presented.

Furthermore, the film thickness calculated through the fitted cubic functions is shown in Fig 8(b), and the film thickness measured by the digital microscope is set as the ground truth to evaluate the accuracy of the detector. All together 91 data points of ice and water test conditions were collected. The data suggest that within 5 mm film thickness, the error of measurement is less than 0.5 mm, and the film thicker than 5 mm will suffer the error of about 1 mm.

As a result, the detector is proved to be capable of identifying dry, water, ice, slush, snow and ice covered with snow conditions with promising accuracy, and the ice and water film measurement precision is better than 0.5 mm when the thickness is within 5 mm.

This test is an experiment before applying the detector on the road to a larger scale. It partially verifies the measuring ability of the detector in the range of predictable road conditions. The combination of sensors brings much more information about the road condition from two different perspective. Thus, it makes the output robust enough for accurate recognition.

In the real application, generally, three or four detectors are installed at intervals of about ten meters, and these detectors are grouped for reliable detection of road surface condition on this very segment of road. This is an effective method to avoid false alarm and missed alarm for the embedded detector can only detect the condensation on its upper surface and the road conditions are not always the same in every parts of the road. The

detector groups are set in the most dangerous areas of the road and the interval is about a few kilometers. The data of the detectors are transferred over RS485 bus in Modbus protocol, every detector owns a unique address and the host polls the detectors. According to the application experience, this detector and similar embedded detectors can work for at least 3 years on the highway, and the service life depends on the traffic flow and the surface subsidence. Low hardware cost guarantees the advantage of widespread application.

On the other hand, the application of non-contact detectors are always limited by cost and the installation interval is about dozens of kilometers or more. Even though non-contact detectors can measure a relatively large area, it's hard to say that one non-contact detector is more reliable than a group of distributed embedded detectors. The price of four embedded detectors are even cheaper than the non-contact detector from the perspective of application. As for the functions, in fact, the relationship between non-contact detectors and embedded detectors is complementary. The detection area of the embedded detector, for instance, our detector, is limited to the upper surface of the detector. This disadvantage is hard to make up, and the best solution is to combine the non-contact detector with the embedded detector, so that the key areas can be closely monitored and the widest range of monitoring can be achieved.

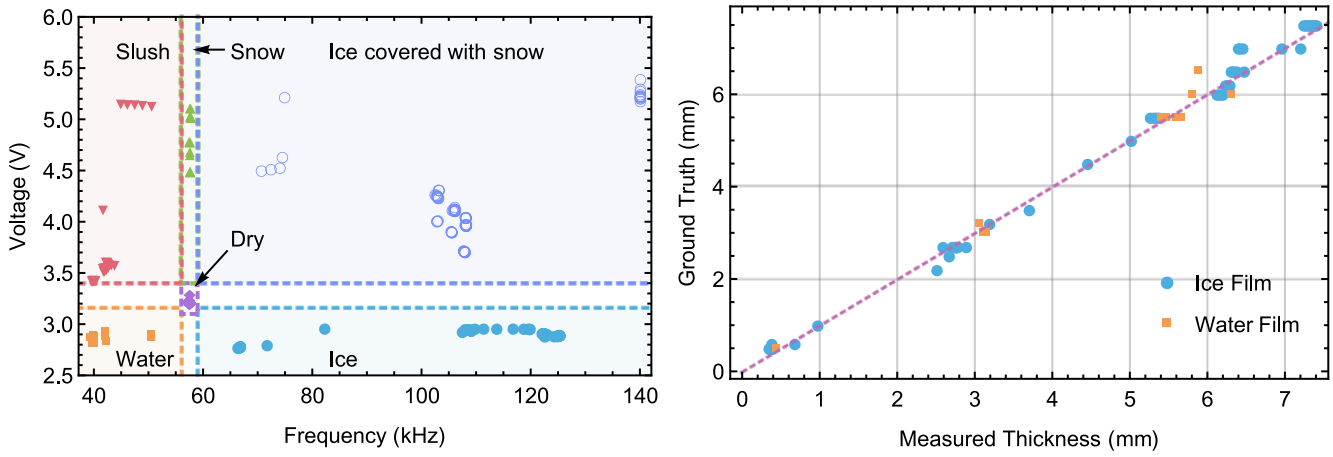

(a) (b)

Figure 8. (a) Data collected in the validation test, the data points fit in the correct data fields divided through the classification table. (b) Measured film thickness based on the fitted cubic functions, and the ground truth was obtained with the digital microscope.

Conclusion

This research work has gone one step further based on the previous study of utilizing piezoelectric sensor for ice and water film thickness measurement. It is an innovation on the application of the piezoelectric sensor and the reflection type optical sensor. The combination of these two sensors extends the function of each other. The road condition detector achieves the goal of classifying six road conditions (dry, water, dry snow, slush, ice, ice covered with snow) and measuring ice and water film thickness with the upper limit higher than 5 mm. More importantly, the successful application of the sensor fusion method on the road condition detector suggests that more elements can be integrated into the detector for richer functionality such as road surface friction estimation.

On the other hand, although the detector has survived the outdoor test and the results are promising, there still exist limitations. The classification table is generated on the basis of experimental data without unexpected conditions, and the threshold values show acute dependence on the border point of the data set. Thus, the iteration work will be testing more proper classification models for more data, such as clustering models and neural networks.

Acknowledgment

This work was supported by the Regional Research Fund Inland of Norway [Grant No. 271758]; the National Natural Science Foundation of China [Grant No. 61104202], and the scholarship from China Scholarship Council and the Research Council of Norway. The authors wish to thank Ms. Ivy and the anonymous reviewers for their valuable comments and suggestions which lead to an improvement of this paper.

References

[1] Perez A P, Wåhlin J, Klein-Paste A. Effect of surface roughness and chemistry on ice bonding to asphalt aggregates[J]. Cold Regions Science & Technology, 2015, 120:108-114. https://doi.org/10.1016/j.coldregions.2015.08.015

[2] Andersson A K, Chapman L. The impact of climate change on winter road maintenance and traffic accidents in West Midlands, UK[J]. Accident; analysis and prevention, 2011, 43(1):284-9. https://doi.org/10.1016/j.aap.2010.08.025

[3] Vignisdottir H R, Booto G K, Bohne R A, et al. Life cycle assessment of anti-and de-icing operations in Norway[C]// Cib World Building Congress. 2016.

[4] Ratkevičius T, Laurinavičius A, Tuminienė F, et al. Reduction of negative impact of salts used for winter road maintenance on the environment[C]// The International Conference on Environmental Engineering. 2014. https://doi.org/10.3846/enviro.2014.165

[5] Casselgren J, Rosendahl S, Sjödahl M, et al. Road condition analysis using NIR illumination and compensating for surrounding light[J]. Optics & Lasers in Engineering, 2016, 77:175-182. https://doi.org/10.1016/j.optlaseng.2015.08.002

[6] Jonsson P, Casselgren J, Thornberg B. Road surface status classification using spectral analysis of NIR camera images[J]. Sensors Journal IEEE, 2015, 15(3):1641-1656. https://doi.org/10.1109/JSEN.2014.2364854

[7] Kutila M , PyykÖNen P , Casselgren J , et al. Road condition monitoring[M]// Computer Vision and Imaging in Intelligent Transportation Systems. John Wiley & Sons, Ltd, 2017. https://doi.org/10.1002/9781118971666.ch15

[8] Colace L, Santoni F, Assanto G. A near-infrared optoelectronic approach to detection of road conditions[J]. Optics & Lasers in Engineering, 2013, 51(5):633-636. https://doi.org/10.1016/j.optlaseng.2013.01.003

[9] Ryu S, Kim T, Bae E. Algorithm and experiment for vision-based recognition of road surface conditions using polarization and wavelet transform[J]. J Emerg Trends Comput Inf Sci, 2014, 5(10): 739-745.

[10] Jonsson P . Classification of road conditions: from camera images and weather data[C]// IEEE International Conference on Computational Intelligence for Measurement Systems & Applications. IEEE, 2011. https://doi.org/10.1109/CIMSA.2011.6059917

[11] Tabatabai H, Aljuboori M. A novel concrete-based sensor for detection of ice and water on roads and bridges[J]. Sensors, 2017, 17(12). https://doi.org/10.3390/s17122912

[12] Troiano A, Pasero E, Mesin L. New system for detecting road ice formation[J]. IEEE Transactions on Instrumentation & Measurement, 2011, 60(3):1091-1101. https://doi.org/10.1109/TIM.2010.2064910

[13] Flatscher M, Neumayer M, Bretterklieber T. Maintaining critical infrastructure under cold climate conditions: A versatile sensing and heating concept[J]. Sensors and Actuators A: Physical, 2017, 267: 538-546. https://doi.org/10.1016/j.sna.2017.09.046

[14] Jackson D G, Liao J Y, Severson J A. An assessment of goodrich ice detector performance in various icing conditions[R]. SAE Technical Paper, 2003. https://doi.org/10.4271/2003-01-2115

[15] Ikiades A A, Armstrong D J, Howard G. Optical diffusion and polarization characteristics of ice accreting in dynamic conditions using a backscattering fibre optic technique[J]. Sensors and Actuators A: physical, 2007, 140(1): 43-50. https://doi.org/10.1016/j.sna.2007.06.009

[16] Amiropoulos K, Spasopoulos D, Ikiades A. Fiber optic sensor for ice detection on aerodynamic surfaces using plastic optic fiber tapers[C]//Optical Sensors. Optical Society of America, 2018: SeM4E. 6. https://doi.org/10.1364/SENSORS.2018.SeM4E.6

[17] Roy S, Izad A, Deanna R G, et al. Smart ice detection systems based on resonant piezoelectric transducers[J]. Sensors and Actuators A Physical, 1998, 69(3):243-250. https://doi.org/10.1016/S0924-4247(98)00101-0

[18] Li X, Wan Y S, Vartuli J, et al. Detection of water-ice transition using a lead zirconate titanate/brass transducer[J]. Journal of Applied

Physics, 2002, 92(1):106-111. https://doi.org/10.1063/1.1481191

[19] Gui K, Ge J, Ye L, et al. The piezoelectric road status sensor using the frequency scanning method and machine-learning algorithms[J]. Sensors and Actuators A: Physical, 2019, 287: 8-20. https://doi.org/10.1016/j.sna.2018.12.048

Kang Gui received the B.S. degree in measurement and control technology and instrumentations from Huazhong University of Science and Technology, Wuhan, Hubei, China, in 2013, where he is currently pursuing the Ph.D. degree. His research interests are in road status sensors, multi-sensor data fusion, deicing system and road weather information system.

Lin Ye received the B.S. and M.S. degrees from Huazhong University of Science and Technology, Wuhan, Hubei, China, in 1982 and 1988, respectively, both in measurement technology and instrumentations. From 1992 to 1993, he was a visiting scholar at Department of Automation, Moscow Institute of Power Engineering, Moscow, Russia. And from 1998 to 1999, he was a visiting scholar at Department of Aeronautics and Astronautics, Washington University, Washington, USA. From 2004, he has been a Professor with the School of Artificial Intelligence and Automation, HUST. His current research area covers ice sensors, aircraft deicing system, in-situ emissivity measurement and non-contact temperature measurement.

Junfeng Ge received the B.S. degree in measurement and control technology and instrumentations from Huazhong University of Science and Technology, Wuhan, Hubei, China, in 2003. He received the M.S. and Ph.D. degrees in control science and engineering from Tsinghua University, Beijing, China, in 2005 and 2009, respectively. He is currently an Associate Professor with the School of Artificial Intelligence and Automation, HUST. His research interests include ice detection, pattern recognition and instrumentation.

Faouzi Alaya Cheikh received the B.S. degree in electronics from ENIT, Tunisia, in 1992. He received the M.S. and Ph.D. degrees in signal processing from Tshwane University of Technology, South Africa, in 1997 and 2004, respectively. He is currently a professor with the Department of Computer Science, NTNU. His research interests include e-Learning, 3D imaging, image and video processing and analysis, video-surveillance, biometrics, video-guided intervention, and content-based retrieval. He is member of the Norwegian Colour and Visual Computing Laboratory (Colourlab).

Lizhen Huang received the B.S. and the M.S. degrees in civil engineering from Chongqing Jiaotong University of Science, Chongqing, China, in 2000 and 2003, respectively. She received the Ph.D. degrees in management science from Tongji University, Shanghai, China, in 2006. She is currently an Associate Professor with the Department of manufacturing and civil engineering, NTNU. Her research interests include sustainable built environment with digitalization and sustainability assessment.